
Article:
Lorinczi, P, Burns, AD, Lesnic, D et al. (4 more authors) (2017) Modelling of gas flow in shale using a finite volume method. Applied Mathematical Modelling, 49. pp. 394-414. ISSN 0307-904X

https://doi.org/10.1016/j.apm.2017.05.009

Modelling of Gas Flow in Shale using a Finite Volume Method

Piroska Lorinczi*[1], Alan D. Burns[2], Daniel Lesnic[3], Quentin J. Fisher[1], Anthony J. Crook[1], Carlos Grattoni[1], Konstantin Rybalcenko[1], [1]Centre for Integrated Petroleum Engineering and Geoscience, School of Earth and Environment, University of Leeds, Leeds, UK; [2]School of Chemical and Process Engineering, University of Leeds, Leeds, UK; [3]Department of Applied Mathematics, University of Leeds, Leeds, UK.

Abstract

Gas flow in shale is a very complex phenomenon, currently investigated using a variety of techniques including the analysis of transient experiments conducted on full core and crushed shale using a range of gases. A range of gas flow mechanisms may operate in shale including continuum flow, slippage, transitional flow and Knudsen diffusion. These processes, as well as gas sorption, need to be taken into account when interpreting experimental data and extrapolating the results to the subsurface. Several models have been published that attempt to account for these different processes. Unfortunately, these have a large number of unknown parameters and few studies have assessed the extent to which transient experiments may be used to invert for the key unknowns or the errors that are associated. Here we present a methodology in which various inversion techniques are applied to assess the viability of deriving key unknowns which control gas flow in shale from transient experiments with a range of noise. A finite volume method is developed for solving the model of Civan (2010, 2011a,b) of transient gas flow in shale. The model is applicable to non-linear diffusion problems, in which the permeability and fluid density both depend on the scalar variable, pressure. The governing equation incorporates the Knudsen number, allowing different flow mechanisms to be addressed, as well as the gas adsorption isotherm. The method is verified for unsteady-state problems for which analytical or numerical solutions are available. The method is then applied to a pressure-pulse decay test. An inverse numerical formulation is generated, using a minimisation iterative algorithm, to estimate some unknown physical parameters. Both numerically simulated noisy and experimental data are input into the formulation of the inverse problem. Error analysis is undertaken to investigate the accuracy of results. A good agreement between inverted and exact parameter values is obtained for several parameters. However, it was found that the strong correlation between intrinsic permeability and tortuosity meant that it was not possible to accurately invert simultaneously for these two parameters from the current pressure-pulse decay model.

1. Introduction

Gas production from shales has revolutionized the USA gas market over the last decade and has been the topic of investigations of many recent studies. However, gas flow in shale seems to be a complex phenomenon that is still not entirely understood. The pores in shales are very small, at the scale of nanometers (Javadpour, 2009), which means that different gas transport mechanisms occur than in rocks with larger pores. In general, either the continuum or the molecular approaches can be used for modelling fluid flow through micro scale channels. Macroscopic fluid properties can be found using the continuum approach. However, on a small scale of physical systems, the validity of the standard continuum approach with no-slip boundary conditions reduces (Roy, 2003). The degree of appropriateness of the continuum model is determined by a dimensionless parameter, the Knudsen number, Kn, which is defined as the ratio of the fluid mean-free-path of molecules λ and the macroscopic length scale of the physical system (mean hydraulic radius for example) (Roy, 2003). In porous media, the macroscopic length scale of the physical system is represented by an equivalent hydraulic radius, R_h, so:

$$Kn = \frac{\lambda}{R_h}. \qquad (1)$$

The Knusden number represents a measure of the degree of rarefaction of gases encountered in small flows through narrow channels. The rarefaction effects become more pronounced with an increase in Kn, and eventually the continuum assumption breaks down (Roy, 2003). The fluid flow regimes can be classified, depending on the Knudsen number, into continuum, slip, transitional and free-molecule (Knudsen) flow (Roy, 2003). Continuum flow is characterised by $Kn<0.01$; the ideal gas constant, Darcy's law and the continuum flow assumption all remain valid in this case. For $Kn\geq0.01$, an effective permeability must be considered, to correct for Knudsen diffusion and/or slip flow, leading to a deviation from Darcy's law. The molecular interactions with the porous medium lead to the dependency of the apparent permeability on pressure (Freeman et al., 2011).

Gas flow in shale is currently being investigated using a variety of laboratory techniques including the analysis of transient experiments conducted on core plugs and crushed samples using a range of gases (helium, nitrogen or methane). Determining the permeability of shale is one of the main objectives in experimental methods. Extremely

low permeabilities (i.e. <1 nD) have often been reported for gas shales. For example, Luffel et al. (1993) reported permeabilites of <0.01 nD from shale. The pulse-decay method, introduced by Brace et al. (1968), and investigated by several other authors (Lin, 1977; Hsieh et al., 1981; Neuzil et al., 1981; Chen and Stagg, 1984; Dicker and Smits, 1988; Luffel et al., 1993), is a well-established transient laboratory technique for measuring the permeability of low permeability rocks. Cui et al. (2009) were the first to expand the pulse-decay method with consideration for gas adsorption. The pulse-decay method has also been used when including the Klinkenberg effect (Jones, 1972; Janot et al., 2007; Janot et al., 2008).

Shale gas flow has been investigated using several modelling approaches. A comparison between different methods for quantifying non-Darcy flow in shale nanopores is presented in Swami et al. (2012). The effects of no-slip and slip flow, Knudsen diffusion, and Langmuir desorption on shale-gas production are considered by Shabro et al. (2011a,b). Civan et al. (2011a,b, 2012) have introduced a theoretically improved model to incorporate all gas flow mechanisms in shale. Their model is based on the Beskok and Karniadakis (1999) unified model for gas flow in micro-tubes, which is valid over the whole range of flow regimes. The unified model of Beskok and Karniadakis (1999) was also used by Florence (2007) to create an improved model to estimate the Klinkenberg-corrected permeability using single-point steady measurements of low permeability sands. Sakhaee-Pour and Bryant (2012) investigated the implications of adsorbed layers of methane and gas slippage at pore walls on the shale gas flow behaviour.

The increased complexity of gas flow within shales means that these models have more unknown parameters than simply the permeability constant needed to describe the Darcy flow. This means that more experiments and more complex inversion schemes are needed to determine key parameters that affect gas flow in shale. Overall, current publications appear to concentrate more on developing new models for gas flow in shales and less on the practicalities of using these models to derive the parameters needed for experimental data for forward modelling. As a first step to addressing this imbalance, the current paper presents a methodology in which various inversion techniques are applied to assess the viability of deriving key unknowns, which control gas flow in shale from transient noisy measurements. The paper begins by presenting a finite volume method (FVM) to solve the nonlinear mathematical model for gas flow in shale presented by Civan et al. (2011 a,b, 2012). The method is applicable to non-linear diffusion problems, in which the permeability and fluid density both depend on the pressure. The governing equation incorporates the Knudsen number, allowing different flow mechanisms to be addressed, as well as the gas adsorption isotherm. Various methods are then presented to invert experimental data for 1, 2 and >2 unknowns. These are first tested on synthetic numerically simulated data with varying amounts of noise before being applied to real experimental data.

To summarise, the main novelties and highlights of our paper are as follows:

- The gas shale model for pressure pulse-decay tests given in the papers by Civan et al. (2011a,b) has been revisited. We have tried to explain the gas shale model more clearly and rigorously and to ensure that the appropriate inverse method of minimisation is correctly applied.
- A new FVM for solving numerically the direct problem for the nonlinear parabolic diffusion equation with pressure dependent permeability subject to boundary conditions of the fourth-kind has been developed and tested.
- The inverse method of minimisation has employed the NAG routine E04FCF. This is robust and shows some independence of the initial guess for the sought parameters.
- We invert for three new parameters, namely the reference coefficients characterising the shale intrinsic permeability and tortuosity. A sensitivity study is also performed prior to inversion.
- New experimental data obtained from our laboratory tests are inverted in order to add practical significance to our study.

2. Experimental Method Setup

Pressure-pulse decay tests are performed in this study. The equipment consists of an upstream and a downstream reservoir and a core holder in which a cylindrical sample (core plug) of length L(m) is placed. **Figure 1** shows a schematic diagram of a pressure pulse-decay test, see also Figure 1 of Civan et al. (2011a). The Cartesian distances in the horizontal flow direction of the two sample ends correspond to x=0 and x=L, respectively. The upstream and downstream reservoir volumes are denoted by V_u and V_d, respectively. The gas used in the experiments investigated in Section 9 is Helium.

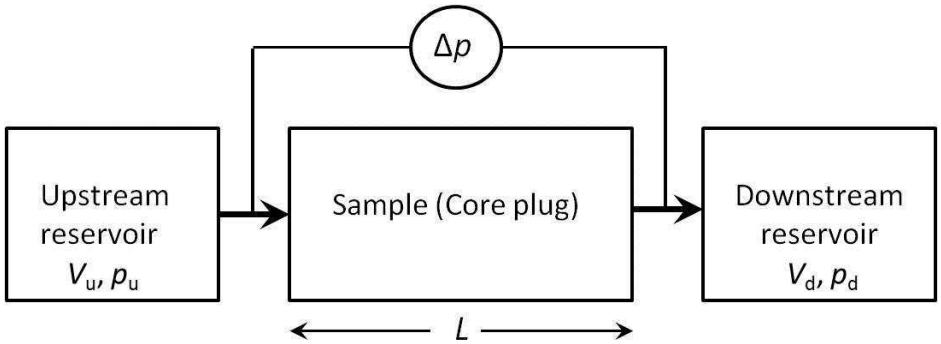

Figure 1. Schematic diagram of a pressure pulse-decay test. L represents the sample length; V_u and V_d denote the upstream and downstream reservoir volumes, and p_u and p_d denote the pressures in the upstream and downstream reservoirs.

Initially, a uniform pressure p_0 applies throughout the system. The test is initiated by applying an increased pressure in the upstream reservoir, denoted by p_u, which is greater than the pressure in the downstream reservoir, denoted by p_d. Therefore, flow occurs from the upstream gas reservoir to the downstream gas reservoir. The upstream and downstream pressures are recorded in time using pressure transducers. A high precision transducer (i.e. 0.01% precision) is used to record the upstream gas pressure and a regular pressure transducer (0.1% precision) is used to record the downstream gas pressure. A confining pressure is applied to the sample; this was set to 1000psi in this study. The confining pressure is monitored using an additional pressure transducer. The temperature is maintained constant at 21°C.

3. Apparent Gas Permeability

When replacing the expression of the mean-free-path of molecules λ and of hydraulic radius R_h in Equation (1), the Knudsen number can be written as (Civan et al., 2011a):

$$Kn = \frac{\mu}{4p}\sqrt{\frac{\pi R_g T \phi}{M_g \tau_h K_\infty}}, \tag{2}$$

where μ is the viscosity of gas, p is the absolute gas pressure, R_g=8314.4 J/kmol K is the universal gas constant, T is the absolute temperature, ϕ is the porosity of porous medium, M_g is the molecular mass of gas, τ_h is the tortuosity and K_∞ is the intrinsic permeability of the tight porous medium.

Tortuosity is a measure of the sinuosity and interconnectedness of the pore space as it influences transport processes through porous media, and it is influenced by the different flow regimes and hence gas pressures (Clennell, 1997).

The permeability measured based on a Darcy-type gradient law by flowing a working-fluid (e.g. He, N_2 or CH_4) through low-permeability rock samples is the apparent permeability and not the intrinsic permeability (Civan et al., 2011a). The apparent gas permeability of gas-bearing shale can be related to the intrinsic permeability via the following relationship (Beskok and Karniadakis, 1999):

$$K = K_\infty f(Kn), \tag{3}$$

where f(Kn) is a flow condition function given in terms of the Knudsen number, the dimensionless rarefaction coefficient α and the slip coefficient b:

$$f(Kn) = (1 + \alpha Kn)\left(1 + \frac{4Kn}{1 - bKn}\right). \tag{4}$$

Civan (2010) introduces an empirical correlation of the form:

$$\frac{\alpha_0}{\alpha} - 1 = \frac{A}{Kn^B}, \quad A > 0, B > 0, \tag{5}$$

where A and B are empirical fitting constants and α_0 is an asymptotic limit value of the dimensionless rarefaction coefficient α ($0 < \alpha < \alpha_0$). The values of these empirical constants are taken in this paper to be the same as the values used in Civan (2010), Civan et al. (2011a, b), namely: α_0=1.358, A=0.178, and B=0.4348. These fitting constants were estimated by Civan (2010) for the special sets of data of Loyalka and Hamoodi (1990). A detailed discussion on the determination of dimensionless rarefaction coefficient α is presented in Beskok and Karniadakis (1999).

4. Gas Adsorption

In the shale gas flow process, some of the gas remains absorbed in shale.

The mass of gas adsorbed per solid volume is given by:

$$q = \frac{\rho_s M_g}{V_{std}} \frac{q_L p}{p_L + p}, \tag{6}$$

where q_L and p_L are Langmuir volume and pressure, respectively, ρ_s is the density of porous sample, M_g is the molecular weight of gas, and V_{std} is the molar volume of gas at standard pressure and temperature (i.e. 273.15 K and 101,325 Pa).

5. Governing Equations

5.1. Mathematical Formulation

To derive the governing equation for shale gas single-phase flow, the conservation of mass and of momentum equations of gas flowing through the porous formation are combined to result in, see e.g. Civan et al. (2011a):

$$\frac{\partial}{\partial t}[\rho\phi + (1-\phi)q] = \nabla \cdot \left(\frac{\rho}{\mu}\mathbf{K}\nabla p\right), \tag{7}$$

where ρ and μ denote the density and dynamic viscosity of the flowing gas, respectively, **K** is the apparent permeability tensor of gas shale and t is time.

We neglect the term involving the gravity in this paper, because our applications of interest involve gas flow through small porous material samples used in laboratory tests.

The density of the flowing gas is given by the real-gas equation of state:

$$\rho = \frac{M_g p}{Z R_g T}, \tag{8}$$

where Z is the real gas deviation factor.

Substituting Equations (6) and (8) in Equation (7) leads to:

$$\frac{\partial}{\partial t}\left[\left(\frac{M_g}{Z R_g T}\phi + (1-\phi)\frac{\rho_s M_g}{V_{std}}\frac{q_L}{p_L + p}\right)p\right] = \nabla \cdot \left(\left(\frac{M_g p}{Z R_g T}\frac{\mathbf{K}}{\mu}\right)\nabla p\right). \tag{9}$$

By denoting:

$$\varrho \equiv \frac{M_g}{Z R_g T}\phi + (1-\phi)\frac{\rho_s M_g}{V_{std}}\frac{q_L}{p_L + p} \tag{10a}$$

the so-called apparent flowing gas density and by **Γ** the so-called apparent diffusivity tensor:

$$\mathbf{\Gamma} \equiv \frac{M_g p}{Z R_g T}\frac{\mathbf{K}}{\mu} \tag{10b}$$

Equation (9) simplifies to:

$$\frac{\partial(\varrho p)}{\partial t} = \nabla \cdot (\mathbf{\Gamma}\nabla p). \tag{11}$$

The applications in this paper consider properties of samples in the direction of flow. Consequently, the components of the vector and tensor quantities in the flow direction denoted by x are used in the following leading to the one-dimensional form of Equation (11):

$$\frac{\partial(\varrho p)}{\partial t} = \frac{\partial}{\partial x}\left(\Gamma\frac{\partial p}{\partial x}\right), \tag{12}$$

where Γ represents the scalar apparent diffusivity.

The governing equation obtained and the use of the conservative form of this is the main difference between the approach introduced in this paper and the one by Civan et al. (2011a), who introduced the apparent convective flux term and an apparent transport coefficient. This results in their governing equation being given in terms of both $\frac{\partial p}{\partial x}$ and $\frac{\partial^2 p}{\partial x^2}$. In our formulation, the approach considered is different, in that we use the conservative form of Equation (9).

Equation (12) is the governing diffusion equation with the pressure p as a primary variable to solve for. In this equation, both the apparent flowing gas density ϱ and the scalar apparent diffusivity Γ depend on p.

For convenience in their formulation, Civan et al. (2011a) introduced the following individual isothermal coefficients of compressibility of the fluid viscosity, shale porosity and intrinsic permeability, and fluid density, respectively:

$$\beta_\phi = \frac{1}{\phi}\frac{\partial \phi}{\partial p}, \qquad \phi(p) = \phi_0 \exp\left(\int_{p_0}^{p} \beta_\phi(p)\,\mathrm{d}p\right) \tag{13a}$$

$$\beta_{K_\infty} = \frac{1}{K_\infty}\frac{\partial K_\infty}{\partial p}, \qquad K_\infty(p) = K_{\infty_0} \exp\left(\int_{p_0}^{p} \beta_{K_\infty}(p)\,\mathrm{d}p\right) \tag{13b}$$

$$\beta_\mu = \frac{1}{\mu}\frac{\partial \mu}{\partial p}, \qquad \mu(p) = \mu_0 \exp\left(\int_{p_0}^{p} \beta_\mu(p)\,\mathrm{d}p\right) \tag{13c}$$

$$\beta_{\tau_\mathrm{h}} = \frac{1}{\tau_\mathrm{h}}\frac{\partial \tau_\mathrm{h}}{\partial p}, \qquad \tau_\mathrm{h}(p) = \tau_{\mathrm{h}_0} \exp\left(\int_{p_0}^{p} \beta_{\tau_\mathrm{h}}(p)\,\mathrm{d}p\right) \tag{13d}$$

$$\beta_\rho = \frac{1}{\rho}\frac{\partial \rho}{\partial p} = \frac{1}{p} - \frac{1}{Z}\frac{\mathrm{d}Z}{\mathrm{d}p}, \tag{13e}$$

where p_0 represents the pressure at the initial time. These isothermal coefficients of compressibility are also used in our formulation.

When taking the isothermal coefficients of compressibility for porosity, permeability, viscosity and tortuosity to have approximately constant values, the corresponding properties can be calculated using Equations (13a) − (13d), as follows (Civan et al., 2011a):

$$\phi(p) = \phi_0 \exp\left[\beta_\phi (p - p_0)\right], \quad \beta_\phi \cong \text{const.} \tag{14a}$$

$$K_\infty(p) = K_{\infty_0} \exp\left[\beta_{K_\infty} (p - p_0)\right], \quad \beta_{K_\infty} \cong \text{const.} \tag{14b}$$

$$\mu(p) = \mu_0 \exp\left[\beta_\mu (p - p_0)\right], \quad \beta_\mu \cong \text{const.} \tag{14c}$$

$$\tau_\mathrm{h}(p) = \tau_{\mathrm{h}_0} \exp\left[\beta_{\tau_\mathrm{h}} (p - p_0)\right], \quad \beta_{\tau_h} \cong \text{const.} \tag{14d}$$

and the subscript '0' of the properties indicates some reference some reference values such as defined at a reference pressure. Substituting Equations (14a) − (14d) into Equation (2) leads to the following expression for Kn:

$$Kn = Kn_0 \frac{p_0}{p} \exp[\beta_\mathrm{T}(p - p_0)], \tag{15}$$

where Kn_0 is the Knudsen number evaluated at p_0 and given by

$$Kn_0 = \frac{\mu_0}{4p_0}\sqrt{\frac{\pi R_\mathrm{g} T \phi_0}{M_\mathrm{g} \tau_{\mathrm{h}0} K_{\infty 0}}}, \tag{16}$$

and β_T denotes

$$\beta_\mathrm{T} = \beta_\mu + \frac{1}{2}\left(\beta_\phi - \beta_{\tau_\mathrm{h}} - \beta_{K_\infty}\right). \tag{17}$$

5.2. Initial and Boundary Conditions

Equation (12) needs to be solved subject to initial and boundary conditions.

The initial condition specifies the pressure p everywhere on the domain $0 < x < L$ at time t=0. In this case, the pressure distribution in the sample (rock) is constant and is defined to have a reference value p_0:

$$p = p_0, \quad 0 < x < L, \qquad t = 0. \tag{18a}$$

We also need to specify p(0,0) and p(L,0):

$$p(0,0) = p_{u0}, \tag{18b}$$

$$p(L,0) = p_{d0}. \tag{18c}$$

Dirichlet boundary conditions can be imposed on one side of the sample – either the downstream or the upstream boundary. These are given by:

$$p = p_{\mathrm{u}}(t), \quad x = 0, \qquad t > 0, \tag{19a}$$

$$p = p_{\mathrm{d}}(t), \quad x = L, \qquad t > 0. \tag{19b}$$

At the other face of the sample, conservation of mass at the sample-reservoir interface is applied. The upstream or the downstream mass-flux boundary conditions are given by (Lin, 1977):

$$\frac{d(\rho V_{\mathrm{u}})}{dt} = -\rho \mathbf{u} \cdot \mathbf{n}\tilde{A}, \quad x = 0, \qquad t > 0, \tag{20a}$$

$$\frac{d(\rho V_{\mathrm{d}})}{dt} = +\rho \mathbf{u} \cdot \mathbf{n}\tilde{A}, \quad x = L, \qquad t > 0, \tag{20b}$$

respectively, where **u** is the volumetric flux vector satisfying Darcy's law, **n** represents the unit vector normal to the open core flow surface and $\tilde{A} = V_{\mathrm{p}}/(\phi L)$, where V_{p} is the effective pore volume of the core sample. Rearranging Equations (20a) and (20b) and considering V_{u} and V_{d} are constant, the following relationships are obtained:

$$\frac{\partial p}{\partial x} = \frac{V_{\mathrm{u}}\mu}{\tilde{A}K}\beta_\rho(p)\,\frac{\partial p}{\partial t}, \quad x = 0, \qquad t > 0 \tag{21a}$$

for the upstream mass-flux boundary condition, and

$$\frac{\partial p}{\partial x} = -\frac{V_{\mathrm{d}}\mu}{\tilde{A}K}\beta_\rho(p)\,\frac{\partial p}{\partial t}, \quad x = L, \qquad t > 0 \tag{21b}$$

for the downstream mass-flux boundary condition.

5.3. Non-dimensional Equations

The governing equation (12) is non-dimensionalised by introducing the following dimensionless variables:

$$\bar{x} = \frac{x}{L}, \quad \bar{t} = \frac{t}{t_0}, \qquad \bar{p} = \frac{p}{p_{\mathrm{s}}}, \qquad \bar{\varrho} = \frac{\varrho}{\varrho_0}, \qquad \bar{\Gamma} = \frac{\Gamma}{\Gamma_0}, \tag{22}$$

where p_s is a scaling pressure, and the subscript '0' of the properties indicates some reference values. In accordance to Equations (10a) and (10b), the properties ϱ and Γ are calculated at the reference pressure as follows:

$$\varrho_0 \equiv \frac{M_{\mathrm{g}}}{Z_0 R_{\mathrm{g}} T}\phi_0 + (1-\phi_0)\frac{\rho_{\mathrm{s}} M_{\mathrm{g}}}{V_{\mathrm{std}}}\frac{q_{\mathrm{L}}}{p_{\mathrm{L}} + p_0} \tag{23a}$$

and

$$\Gamma_0 \equiv \frac{M_{\mathrm{g}} p_0}{Z_0 R_{\mathrm{g}} T}\,\frac{\mathrm{K}_0}{\mu_0}, \tag{23b}$$

respectively.

The apparent gas permeability at the reference pressure is calculated using Equation (3) as

$$K_0 = K_{\infty 0} f(Kn_0). \tag{24}$$

The reference value for time, t_0, is given by:

$$t_0 = L^2 / (\Gamma_0/\varrho_0). \tag{25}$$

In non-dimensional form, Equations (12) becomes:

$$\frac{\partial(\bar{\varrho}\bar{p})}{\partial \bar{t}} = \frac{\partial}{\partial \bar{x}}\left(\bar{\Gamma}\frac{\partial \bar{p}}{\partial \bar{x}}\right). \tag{26}$$

The initial condition given by Equations (18a) – (18c) will become:

$$\bar{p} = \frac{p_0}{p_s}, \quad 0 < \bar{x} < 1, \qquad \bar{t} = 0, \tag{27a}$$

$$\bar{p}(0,0) = \frac{p_{u0}}{p_s}, \tag{27b}$$

$$\bar{p}(1,0) = \frac{p_{d0}}{p_s}, \tag{27c}$$

The Dirichlet boundary conditions (19a) and (19b) become:

$$\bar{p} = \bar{p}_u(t) = p_u(t)/p_s, \quad \bar{x} = 0, \qquad \bar{t} > 0, \tag{28a}$$

$$\bar{p} = \bar{p}_d(t) = p_d(t)/p_s, \quad \bar{x} = 1, \qquad \bar{t} > 0, \tag{28b}$$

and the mass-flux boundary conditions (21a) and (21b) become:

$$\frac{\partial \bar{p}}{\partial \bar{x}} = \frac{V_u(\Gamma_0/\varrho_0)}{\tilde{A}L}\frac{\mu}{K}\beta_\rho(\bar{p})\frac{\partial \bar{p}}{\partial \bar{t}}, \quad \bar{x} = 0, \quad \bar{t} > 0, \tag{29a}$$

$$\frac{\partial \bar{p}}{\partial \bar{x}} = -\frac{V_d(\Gamma_0/\varrho_0)}{\tilde{A}L}\frac{\mu}{K}\beta_\rho(\bar{p})\frac{\partial \bar{p}}{\partial \bar{t}}, \quad \bar{x} = 1, \quad \bar{t} > 0. \tag{29b}$$

6. Finite Volume Method

The finite volume method (FVM) (or control volume method, CVM) is a numerical technique well-suited for the simulation of various types of conservation laws (Patankar, 1980). When the integral conservation law is enforced for each control volume, a linear algebraic system is obtained by numerical integration of the conserved variables over the volume. If we denote by δx the spatial step size and by δt the time step size, then the conservative finite volume discretisation of the non-dimensional Equation (26) (when using an implicit time-stepping and dropping the overbars for simplicity) is:

$$\begin{aligned}\frac{(\varrho p)_i^{n+1} - (\varrho p)_i^n}{\delta t} &= \frac{1}{\delta x}\left[\left(\Gamma\frac{\partial p}{\partial x}\right)_{i+\frac{1}{2}}^{n+1} - \left(\Gamma\frac{\partial p}{\partial x}\right)_{i-\frac{1}{2}}^{n+1}\right] \\ &= \frac{1}{\delta x}\left[\Gamma_{i+\frac{1}{2}}^{n+1}\left(\frac{p_{i+1}^{n+1} - p_i^{n+1}}{\delta x}\right) - \Gamma_{i-\frac{1}{2}}^{n+1}\left(\frac{p_i^{n+1} - p_{i-1}^{n+1}}{\delta x}\right)\right] \\ &= \frac{1}{(\delta x)^2}\left[\Gamma_{i+\frac{1}{2}}^{n+1}(p_{i+1}^{n+1} - p_i^{n+1}) - \Gamma_{i-\frac{1}{2}}^{n+1}(p_i^{n+1} - p_{i-1}^{n+1})\right],\end{aligned} \tag{30}$$

where the subscript i denotes a spatial step, i=1,..., N_x, and the superscript n denotes a time step, n=0,.., N_t-1, with N_x and N_t representing the number of control volumes, and of time steps, respectively.

The discretisation of the governing equation over the control volumes results in a non-linear system to be solved at each time step. Therefore, an iterative non-linear solver is required at each time step. At each iteration, the system is linearized by evaluating the pressure-dependent diffusion coefficients $\Gamma_{i\pm\frac{1}{2}}$ at the current pressure values.

The subsequent linearized system is solved using a tri-diagonal matrix algorithm. The coefficients are recomputed and the system is solved again, until convergence is achieved. Furthermore, since the apparent flowing gas density ϱ and the scalar apparent diffusivity Γ depend on the primary variable p, both these properties are evaluated at each iteration using the pressure value at the previous iteration (which is the initial time for the first iteration at the first time step).

The real gas deviation factor Z is evaluated in each control volumes for each time step, using the improved correlation developed by Al-Anazi and Al-Quraishi (2010). The apparent flowing gas density ϱ can therefore be

calculated from Equation (10a) at each time step. To calculate the apparent scalar diffusivity Γ, the value of Kn is determined first at each time step using Equation (15), then the dimensionless rarefaction coefficient α can be determined using Equation (5). This allows the calculation of the flow condition function f(Kn) at each time step, using Equation (4) and then the apparent permeability K, using Equation (3). Therefore, the apparent scalar apparent diffusivity Γ can be calculated at each time step using Equation (10b).

The boundary conditions are also evaluated at each iteration, since they depend on the primary variable, p. The isothermal coefficients of compressibility of fluid density $\beta_\rho(\bar{p})$ needed in the mass-flux boundary conditions (29a) and (29b) are calculated using Equation (13e), with the values of Z determined and the corresponding pressure values. The resulting linearised equation is solved at each iteration and the solution p at the current time step is used to update the properties and boundary conditions at the next time step. The procedure is repeated until the desired time has been reached. In case of a steady-state problem, the number of time steps is taken to be one ($\delta t = \infty$ leading to $1/\delta t = 0$), and the procedure is applied only once, using several iterations to achieve convergence.

7. Direct Solution

7.1. Verification of Numerical Approach

The developed numerical approach can also be applied for problems governed by the diffusion Equation (12), in which the properties ϱ and Γ do not depend on the primary variable p. The boundary conditions have been implemented to have the general form:

$$A_0 p + A_1 \frac{\partial p}{\partial x} + A_2 \frac{\partial p}{\partial t} = B_0 \tag{31}$$

with A_i, i=0,1,2 and B_0 are coefficients which are either constants or variable and they can depend on p, such that the algorithm can handle different boundary condition types.

Example 7.1.

The approach was first tested on the diffusion equation:

$$\frac{\partial^2 \bar{p}}{\partial \bar{x}^2} = \frac{\partial \bar{p}}{\partial \bar{t}}, \quad 0 < \bar{x} < 1, \quad \bar{t} > 0 \tag{32}$$

with initial and boundary conditions in the non-dimensional form given by:

$$\bar{p} = 0, \quad 0 < \bar{x} \leq 1, \quad \bar{t} = 0, \tag{33a}$$

$$\bar{p}(0,t) = 1 \text{ and } \bar{p}(1,\bar{t}) = 0, \ \bar{t} > 0. \tag{33b}$$

This problem has an analytical solution available (Al-Dhahir and Tan, 1968); mesh independence of our numerical FVM was checked and ensured and moreover, when compared with the analytical solution, percentage error is decreasing when using finer meshes from very early times (see Table 1). Furthermore, an excellent agreement between the numerical and analytical solutions was obtained for Example 7.1 for later times (Figure 2).

N_t	25		50		100	
N_x	Solution	Percentage error (%)	Solution	Percentage error (%)	Solution	Percentage error (%)
51	0.0856	8.34	0.0852	7.90	0.0843	6.64
101	0.0833	5.48	0.0826	4.63	0.0815	3.12
201	0.0820	3.76	0.0811	2.70	0.0799	1.06
Analytical	0.0790		0.0790		0.0790	

Table 1. Comparison between the numerical FVM solution and analytical solution for p(0.5,0.04) for various meshes obtained using N_x=51, 101 and 201 respectively, and N_t=25, 50 and 100 respectively, with the corresponding percentage errors, for Example 7.1.

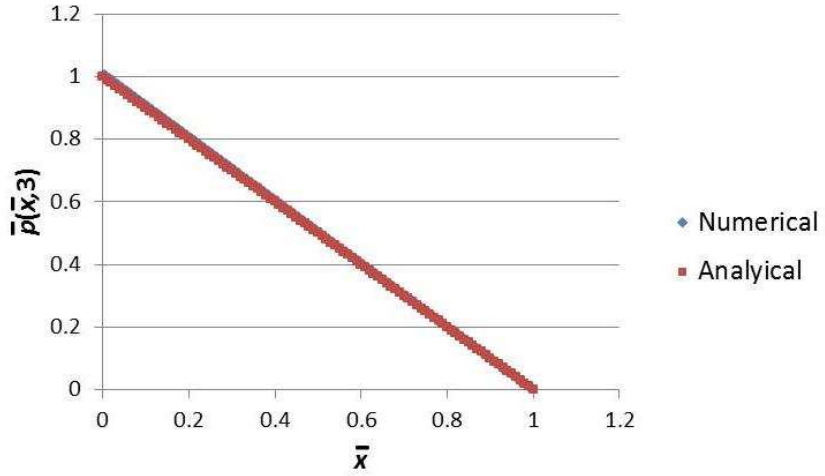

Figure 2. Numerical and analytical solutions for Example 7.1 obtained for N_x=101 and N_t=100, at the non-dimensional time $\bar{t} = 3.0$ for $0 \leq \bar{x} \leq 1$.

Example 7. 2

In the second example we consider solving the diffusion equation:

$$\bar{\varrho}\frac{\partial \bar{p}}{\partial \bar{t}}(x,t) = \bar{\Gamma}\frac{\partial^2 \bar{p}}{\partial \bar{x}^2}; \qquad (\bar{x},\bar{t}) \in (0,1) \times (0,1], \tag{34}$$

where $\bar{\varrho}$ and $\bar{\Gamma}$ are constants, with initial and boundary conditions (in non-dimensional form) given by:

$$\bar{p}(x,0) = 0, \qquad 0 \leq \bar{x} \leq 1, \quad \bar{t} = 0, \tag{35}$$

$$\bar{p}(1,\bar{t}) = 0, \quad 0 < \bar{t} \leq 1, \tag{36}$$

$$\frac{\partial \bar{p}}{\partial \bar{t}}(0,\bar{t}) = \nu_u \frac{\partial \bar{p}}{\partial \bar{x}}(0,\bar{t}) + \gamma_u, \qquad 0 < \bar{t} \leq 1; \qquad \gamma_u \neq 0. \tag{37}$$

Although this problem has an analytical solution available (Esaki et al., 1996) we compare our numerical results with those presented in Lesnic et al. (1997), who used a weighted finite difference method. **Figure 2a** shows the good agreement achieved from this comparison for the pressure increase curve, p(0,t), when L = 3cm, the mean value of the hydraulic conductivity is 1.35 x 10^{-6}cm/s and a constant inflow rate of 1.6 x 10^{-3}cm^3/s is supplied to the upstream reservoir (see Lesnic et al., 1997 for complete experiment data and notations). Using their data leads to the following values for $\bar{\varrho}$ and $\bar{\Gamma}$:

$$\bar{\varrho} = 1.66 \times 10^{-4} \text{ and } \bar{\Gamma} = 1. \tag{38}$$

The constants in the upstream boundary condition (37) become:

$$\nu_u = 5.424, \quad \gamma_u = 5.33. \tag{39}$$

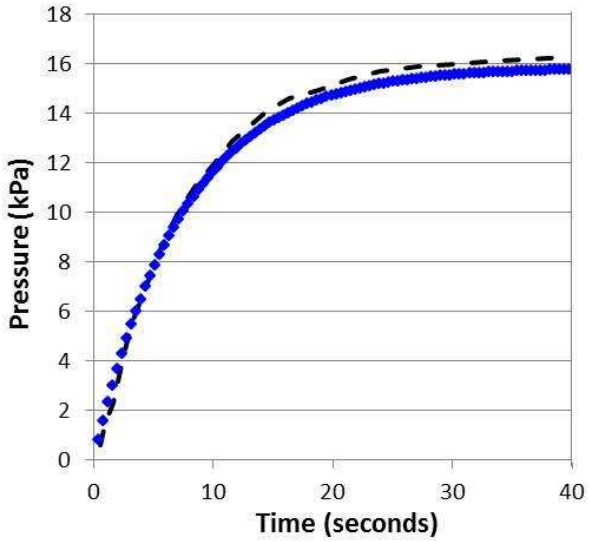

Figure 2a. Numerical results obtained by the FVM (♦♦♦) with N_x=101, N_t=100, and the weighted average finite-difference method presented in Lesnic et al. (1997) (− − − −), for the pressure increase curve, p(0,t), for Example 7.2.

Example 7. 3

Other tests of the FVM include examples in which $\bar{\varrho}$ and $\bar{\Gamma}$ are constant and the boundary conditions are of the type:

$$\bar{p}(x,0) = 0, \qquad 0 < \bar{x} \leq 1, \quad \bar{p}(0,0) = \frac{p_{u0}}{p_s} \neq 0, \tag{40}$$

$$\frac{\partial \bar{p}}{\partial \bar{t}}(0,\bar{t}) = -\nu_u \frac{\partial \bar{p}}{\partial \bar{x}}(0,\bar{t}), \quad 0 < \bar{t} \leq 1, \tag{41}$$

$$\frac{\partial \bar{p}}{\partial \bar{t}}(1,\bar{t}) = \nu_d \frac{\partial \bar{p}}{\partial \bar{x}}(1,\bar{t}), \quad 0 < \bar{t} \leq 1, \tag{42}$$

representing a mathematical model of the transient pulse test designed by Brace et al. (1968), and investigated by Neuzil et al. (1981). In their paper, Neuzil et al. (1981) investigated the conditions of determining hydraulic properties of tight rocks by a graphical method based on analytical solutions to the transient pulse test presented in Hsieh et al. (1981). Numerical results are presented for the case when hydraulic conductivity is 5.2 x 10^{-10} m/s and the dimensionless parameter β, which denotes the ratio of compressive storage in the downstream reservoir to compressive storage in the upstream reservoir is $\beta = 0.2$ (see Neuzil et al., 1981 and Hsieh et al., 1981 for complete experiment data and notations).

Figure 3 shows the numerical results for pressure at the upstream boundary $\bar{p}(0,t)$ (red) and downstream boundary $\bar{p}(1,t)$ (blue) for this example, obtained for N_x=101 and N_t=100, in comparison to the results obtained by the graphical method based on analytical solutions presented in Neuzil et al. (1981). A relatively good agreement between the two sets of solutions is in evidence in this figure.

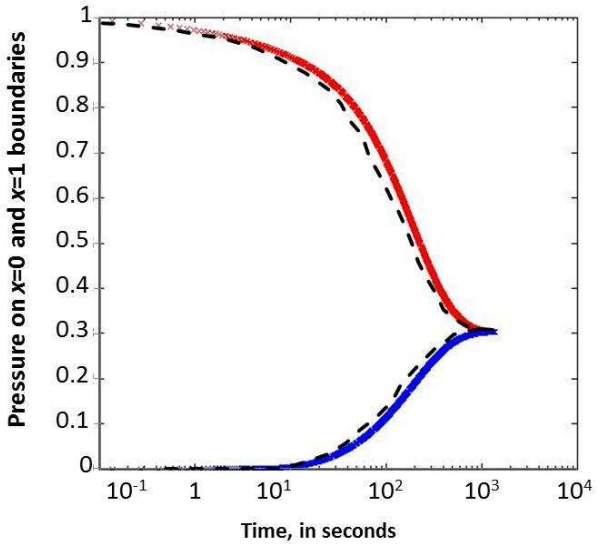

Figure 3. Numerical results obtained by FVM (−−−−) and the graphical method based on analytical solutions presented in Neuzil et al. (1981) (− − − −) when $\beta = 0.2$, for the pressures at the upstream and downstream boundaries, for Example 7.3.

7.2. Experimental Validation Under Steady-State Conditions

Example 7.4

The numerical approach was validated by comparison with the experimental results of Pong et al. (1994) on a steady-state example. The example involves measurements of nitrogen gas pressures during flow through a micro-channel under steady-state conditions. The experimental data are for the inlet pressures p_{u0} of 135kPa, 170kPa, 205kPa, 240kPa and 275kPa, and a constant outlet pressure of 100.8 kPa.

Figure 4 shows the results obtained by the FVM for the five different inlet pressures, obtained with N_x=201, superposed on the numerical and experimental pressure profiles of Civan et al. (2011a) and Pong et al. (1994), respectively. A very good agreement is in evidence between our solution and the other two sets of results, with our results being undistinguishable from the numerical results of Civan et al. (2011a).

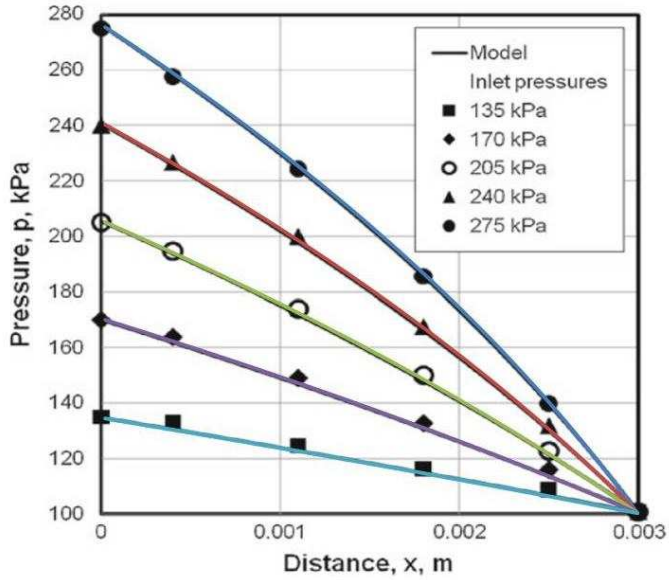

Figure 4. Pressure profiles obtained by FVM (in colour) superposed on the numerical pressure profiles of Civan et al. (2011a) (in black) and the experimental data of Pong et al. (1994) (with markers).

7.3. Numerical Results for Pressure-Pulse Decay Tests

The numerical approach was tested on two pressure-pulse decay tests (unsteady state examples).

Example 7. 5

This example is a numerical simulation of Test #2 from Civan et al. (2011b, 2012). The simulated gas used was the same, namely nitrogen. The upstream reservoir pressure was kept constant during this test, at p_u= 35atm= 3,546,375Pa, that is,

$$p(0,t) = p_u, \quad t > 0, \tag{43}$$

whilst the initial pressure is

$$p(x,0) = p_0, \quad 0 < x < L, \tag{44}$$

where p_0=1atm=101,325 Pa. At the downstream boundary, condition (21b) is applied.

The data was taken as in Table 1 from Civan et al. (2011b); they are also presented in SI units in Appendix A of this paper. This example has the Langmuir gas pressure and volume equal to zero. The reference time t_0 is found from Equation (25) to be 1560.5s.

Figure 5 shows the pressure at the downstream boundary pressure versus time for this test (pressure at upstream boundary kept constant) obtained with N_x=201 and N_t=1000, in comparison with the results presented in Figure 9 of Civan et al. (2011b) and very good agreement can be observed.

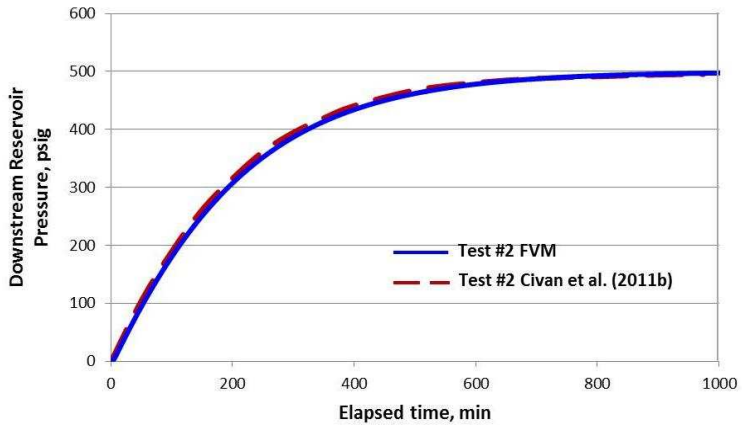

Figure 5. Numerical results for pressure p(L,t) at the downstream boundary x=L obtained by FVM in comparison with the results of Civan et al. (2011b) Test #2 for Example 7.5.

Pressure profiles across length of sample are shown in **Figure 6**. The times at which the pressure profiles were plotted were chosen such that the pressure values at the downstream boundary were very close to those presented by Civan et al. (2011b) in Figure 13 of their paper. However, the time levels (in minutes) necessary for the system to reach these pressure profiles are different from the time levels indicated by Civan et al. (2011b). The difference in times is believed to be due to the computational differences of the two approaches or perhaps some different values for the input data. However, a reduction in the factor between the two sets of times is observed, this gets to 1.32 for the last time level presented (79.6min in our test and 60min in Civan et al., 2011b test).

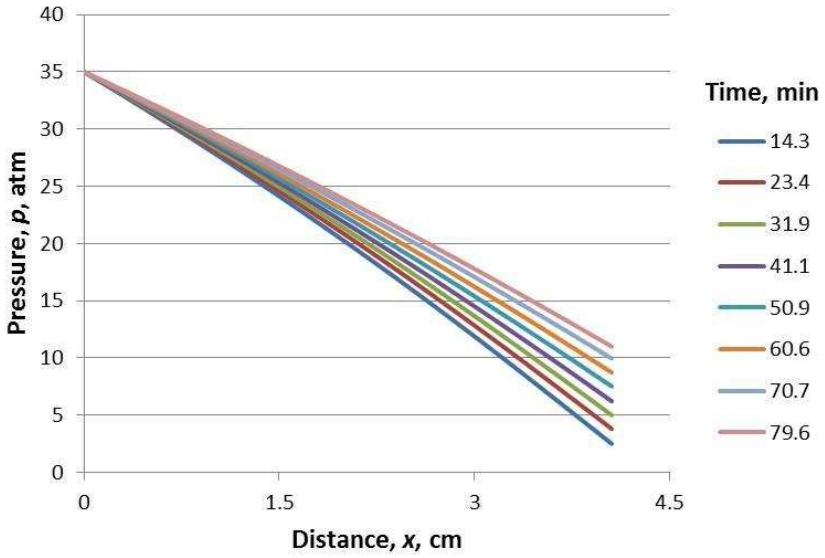

Figure 6. Pressure profiles across the length of sample obtained for Example 7.5. In this figure, t=14.3min corresponds to the lowest curve and the subsequent curves increase monotonically.

Example 7. 6

This example is a numerical simulation of the pressure-pulse decay test presented in Civan et al. (2011), namely flow under transient-state conditions. The same gas is considered, namely methane. The downstream reservoir pressure was kept constant in this example, namely to p_d =101,325Pa, that is,

$$p(L,t) = p_{\mathrm{d}}, \quad t > 0, \tag{45}$$

whilst the initial pressure is given by Equation (44) with p_0 =1atm=101,325Pa. At the upstream boundary $p(0,0) = p_{\mathrm{u}0} = 500\mathrm{kPa}$. Condition (21a) is applied at the upstream boundary.

The other data used are shown in Appendix A of this paper (in SI units), consistent with the data given in Civan et al. (2011a). This example has the Langmuir gas pressure $p_L = 7.5 \times 10^6 \mathrm{Pa}$ and Langmuir gas volume $q_L = 0.01 \mathrm{std\ m^3/kg}$. The reference time t_0 is found from (25) to be 2107.78s.

Pressure profiles across length of sample obtained with N_x=201 and N_t=1000 are shown in **Figure 7**. These profiles were plotted at the same times as the ones given in Civan et al. (2011a) (Figure 3 in their paper). A similar behaviour can be noticed, however the times at which the two sets of profiles are reached are different. The difference in times is believed to be due to some input data being different, as well as to mathematical differences between the solution for p(0,t) when imposing the boundary condition (21a) in our paper, and the boundary condition (57) in Civan et al. (2011a) paper.

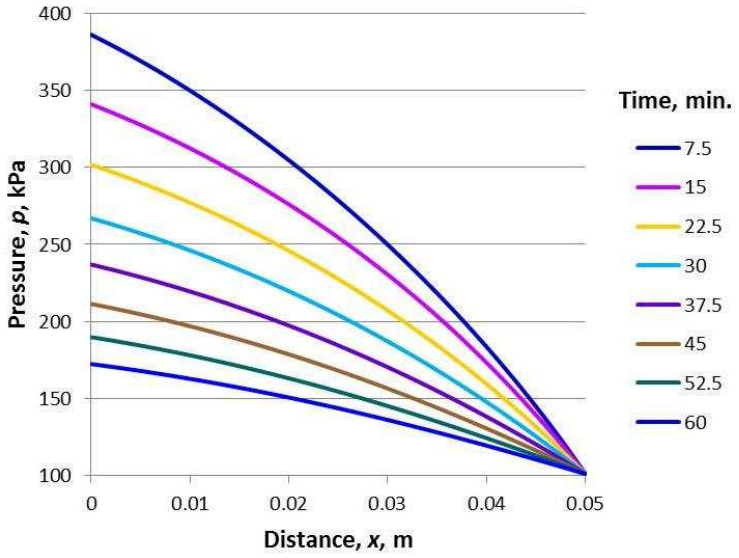

Figure 7. Pressure profiles across the length of sample obtained for Example 7.6 by the FVM.

8. Inverse Problem Formulation

8.1. Known Input Parameters

When running a pressure-pulse decay test, some of the parameters needed in the governing equation are known or can be directly determined. Some of the core sample properties (length, diameter, grain density) are known. The remaining core sample property, the porosity, is determined separately, for example using techniques described in Luffel et al. (1993). Once the porosity is determined, the compressibility coefficient for porosity β_ϕ can be determined using the approach outlined below. A power-law relationship between pore volume compressibility and net effective confining pressure has been experimentally determined from laboratory data from very tight gas sandstones presented by Byrnes et al. (2009):

$$\beta_\phi = 10^{\left(-1.035+0.106/\phi_p{}^{0.5}\right)\times \log_{10} p_e + 4.857\phi_p{}^{-0.0385}}, \qquad (46)$$

where β_ϕ is the pore volume compressibility in 10^6/psi, ϕ_p is the unconfined routine porosity (in %) and p_e is the average net effective confining pressure at which β_Φ applies (in psi). As such, for a net effective confining pressure of p_e =5000psi, and a porosity of ϕ_p = 6%, the compressibility coefficient for porosity β_ϕ = 1.07x10^{-9}Pa^{-1}.

The gas properties (gas type, molecular mass, critical temperature and critical pressure, universal gas constant, viscosity, molar volume of gas at standard temperature and pressure) are known, while the compressibility coefficient for fluid viscosity, β_μ, can be determined using Equation (13c) from the dependence of viscosity on pressure at the prescribed temperature of the core flow tests (see Civan et al., 2011a). The pressure-pulse decay tests conditions, namely: temperature, initial gas pressure, upstream (or downstream) gas pressure, upstream and downstream reservoir volume are all known.

Some of the flow parameter values are also known or can be determined. The Langmuir gas pressure and Langmuir gas volume can be determined by consideration of the adsorption/desorption effects according to Ross and Bustin (2007).

The compressibility coefficient for intrinsic permeability $\beta_{K\infty}$ can be determined using the approach outlined below. A power-law relationship between intrinsic permeability K_∞ (in D), and the net stress has been experimentally determined in our laboratory, of the form:

$$K_\infty(p) = K_0 p^{-E}, \qquad (47)$$

where $K_0 = K_{\infty 0} p_0{}^E$ is the permeability (mD), p is the net stress (psi) and E is a dimensionless constant. This relationship has been determined for values of K_0 > 0.01mD (with E<0).

Using the definition of $\beta_{K\infty}$, given by Equation (13b), and Equation (47) by differentiation with respect to p leads to the following expression of $\beta_{K\infty}$ when K_0 > 0.01mD (with E<0):

$$\beta_{K_\infty}(p) = -\frac{E}{p}. \qquad (48a)$$

For $K_0 < 0.01$mD, E>0 and Equation (48a) is changed to:

$$\beta_{K_\infty}(p) = \frac{E}{p}, \tag{48b}$$

to account for the positive sign of β_{K_∞}.

The dimensionless constant E has been determined to vary between [-2, 2] for K_0 varying between $[10^{-18}, 10^{-4}]$D. When choosing the range $[10^{-18}, 10^{-17}]$D for K_0, the constant E is $E = 0.106$. Then, from (48b), the value of β_{K_∞} for a net stress of p=2000psi is determined to be 7.68×10^{-9} Pa^{-1}.

Therefore, all parameters except the intrinsic permeability $K_{\infty 0}$, tortuosity τ_{h0} and the compressibility coefficient for tortuosity $\beta\tau_h$ are either known or can be determined. The values of these three parameters are obtained using an inverse problem formulation, described in the next section.

8.2. Inverse Problem: Determination of Unknown Parameters

An inverse problem is formulated as follows: minimise the nonlinear least-squares objective function defined as:

$$F(\underline{X}) = \sum_{i=1}^{M} \left[\bar{p}(\underline{X}; 0, \bar{t}_i) - \bar{p}(0, \bar{t}_i)\right]^2, \tag{49}$$

where

$\underline{X} = (K_{\infty 0}, \tau_{h0}, \beta\tau_h)$ is the vector of values for the parameters to be inverted;

$p(\underline{X}; 0, \bar{t}_i)$ is the computed pressure at the upstream boundary $\bar{x} = 0$ obtained by solving the direct problem;

$p(0, \bar{t}_i)$ is the given measured or numerically simulated pressure at the upstream boundary $\bar{x} = 0$;

$\bar{t}_i$ (i=1,..,M) are instants at which the pressure is measured.

In the case of numerically simulated data, in order to avoid an inverse crime, care is taken that the direct and inverse solver have different mesh sizes, e.g. N_x and N_x+1 discretisation points in the direct and inverse problems, respectively.

The function $F(\underline{X})$ is defined for the upstream boundary $\bar{x} = 0$; a similar function can be defined for the downstream boundary $\bar{x} = 1$.

It should be pointed out that this objective function is different from the one given in Civan et al. (2011a, b). The sum of least squares used in their papers is defined in terms of the calculated and measured pressure gradients, rather than the calculated and measured pressures at the sides of the core plug. The pressure gradients used in their sum of least squares are estimated from pressure measurements using finite-difference approximations.

In the remaining of this section we investigate the retrieval of the parameters $K_{\infty 0}$, τ_{h0} and $\beta\tau_h$ for the pressure-pulse decay test described in Example 7.6. We take N_t=1000 and N_x=201.

8.2.1. Sensitivity Analysis

Prior to performing the inverse analysis of identifying all 3 unknown parameters, a sensitivity study was undertaken, by calculating the sensitivity coefficients, as a function of time. Sensitivity coefficients are the first derivatives of the measured quantities, i.e. upstream pressure, with respect to the unknowns, see e.g. Banks et al. (2007). In general, the sensitivity coefficients are desired to be large and uncorrelated.

The sensitivity coefficients are calculated as:

$$S_i(\bar{t}) = \frac{\partial \bar{p}\,(0, \bar{t}, \underline{X})}{\partial X_i} = \frac{\bar{p}(0, \bar{t}; X_1, \ldots, X_i + \Delta_i, \ldots, X_3) - \bar{p}(0, \bar{t}; X_1, \ldots, X_i, \ldots, X_3)}{\Delta_i}, \qquad i = 1,2,3, \tag{50}$$

where $\underline{X} = (X_1, X_2, X_3) = (K_{\infty 0}, \tau_{h0}, \beta_{\tau_h})$ and $\Delta_i = 1\% \times X_i$.

Figure 8 shows the sensitivity coefficients for $K_{\infty 0}$, τ_{h0} and $\beta\tau_h$. As it can be noticed, the sensitivity coefficients for the three parameters are close to zero for $6 \le \bar{t} \le 10$. This indicates that on this time interval the upstream pressure $\bar{p}\,(0, \bar{t})$ does not depend significantly on any of the three parameters. Therefore, our inversion investigation focuses on the initial time $0 \le \bar{t} \le 6$ which offers more useful information for retrieving the

unknowns.

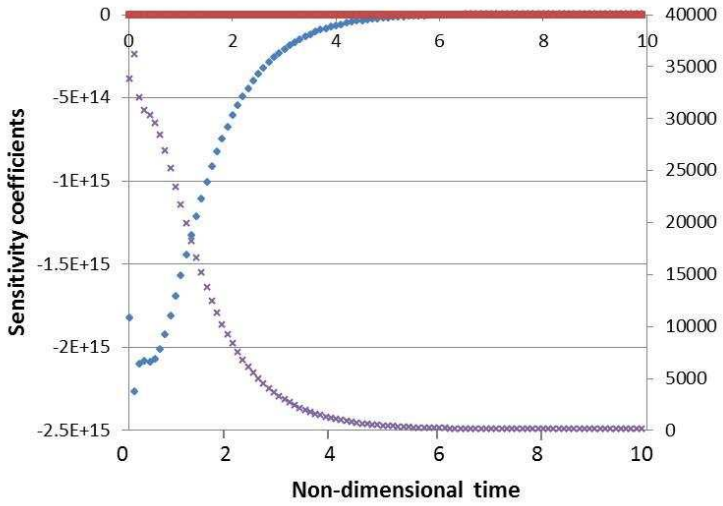

Figure 8. Sensitivity coefficients for: $K_{\infty 0}$ (blue) and τ_{h0} (red) (on primary axis) and $\beta\tau_h$ (lilac) (on secondary axis).

It is also useful to look first at the inversion of a single (Subsection 8.2.2) or a double (Subsection 8.2.3) parameter in order to gain insight into when multiple parameters are inverted.

8.2.2. Inversion for 1 Parameter

The inverse problem was first solved for 1 parameter, i.e. considering only one of the three parameters $K_{\infty 0}$, τ_{h0} and $\beta\tau_h$ to be unknown, while fixing the values of two of the others. The objective function is plotted against a wide range of values of the corresponding parameter which is inverted in Figure 9. In each case a global minimum is obtained at the exact value of the sought parameter.

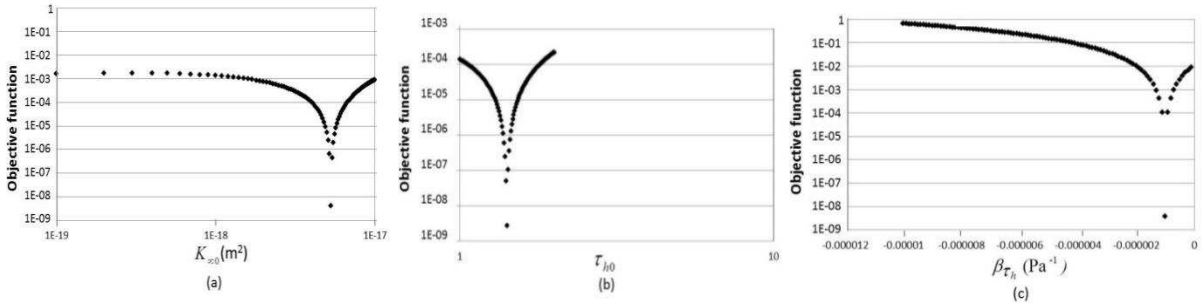

Figure 9. Results for the inversion with 1 parameter, for: (a) $K_{\infty 0}$; (b) τ_{h0} and (c) $\beta\tau_h$ with minima corresponding to: (a) $K_{\infty 0}=5.3\text{x}10^{-18}\text{m}^2$; (b) $\tau_{h0}=1.41$ and (c) $\beta\tau_h=-1.0\ \text{x}10^{-6}\text{Pa}^{-1}$, respectively.

The inverse problem was investigated also for the case when noise is added to the direct problem pressure data $\bar{p}(0,\bar{t})$ in the form:

$$\bar{p}_{\text{noisy}}(0,\bar{t}) = \bar{p}(0,\bar{t}) + \varepsilon, \qquad \bar{t} > 0, \tag{51}$$

where ε are random variables generated from a Gaussian normal distribution with zero mean and standard deviation given by

$$\varepsilon_n\% \times \max_{\bar{t}>0}|\bar{p}(0,\bar{t})|, \tag{52}$$

where $\varepsilon_n\%$ represents the percentage of noise.

Figure 10 shows the solution for the non-dimensional pressure on the upstream boundary $\bar{p}(0,\bar{t})$ (red stars) and the 0.1% noisy data $\bar{p}_{\text{noisy}}(0,\bar{t})$ (blue diamonds).

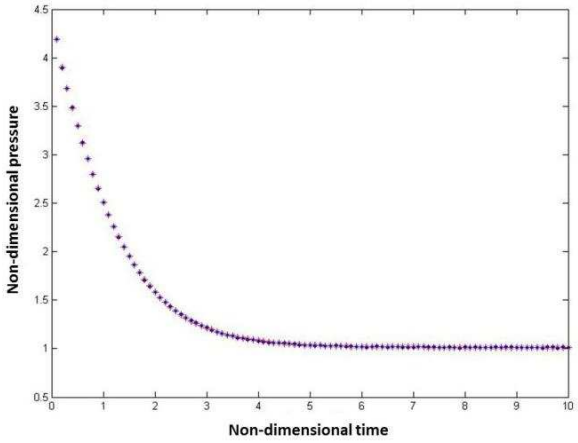

Figure 10. Solution for the non-dimensional pressure on the upstream boundary $\bar{p}(0,\bar{t})$ (red stars) and the 0.1% noisy data $\bar{p}_{\text{noisy}}(0,\bar{t})$ (blue diamonds).

Table 2 shows the numerical results for the inversion of a single parameter $K_{\infty 0}$, τ_{h0} or $\beta\tau_h$ obtained when adding a noise of 0.1% into the data, using Equation (51). It can be seen from this table that a reasonable retrieval of one of the unknowns is obtained. The retrieval of $K_{\infty 0}$ or τ_{h0} is amplified by 5-6% for an input upstream pressure perturbed by 0.1% noise. However, the parameter $\beta\tau_h$ is exactly retrieved. We have also investigated the retrieval of this parameter for higher levels of noise, e.g. 1%, and a good retrieval has been obtained. It means that we can always retrieve this parameter even for higher levels of noisy data.

Parameter/unit	Exact	Numerical	Percentage error (%)
$K_{\infty 0}$ (m^2)	$5.3\text{x}10^{-18}$	$5.6\text{x}10^{-18}$	5.6
τ_{h0}	1.41	1.51	6.7
$\beta\tau_h$ (Pa^{-1})	$-1.0\ \text{x}10^{-6}$	$-1.0\ \text{x}10^{-6}$	0

Table 2. Results for inversion with 0.1% noise for 1 parameter: $K_{\infty 0}$, τ_{h0} or $\beta\tau_h$.

8.2.3. Inversion for 2 Parameters

The inverse problem was then solved for 2 parameters, i.e. considering two of the three parameters $K_{\infty 0}$, τ_{h0} and $\beta\tau_h$ to be unknown, while fixing the value of the other. The objective function is plotted against a wide range of values of the inverted parameters resulting in a three-dimensional surface plot. Results are shown in **Figure 11** for the inversion of τ_{h0} and $\beta\tau_h$ and one can observe that the global minimum is attained at the exact values of the sought parameters.

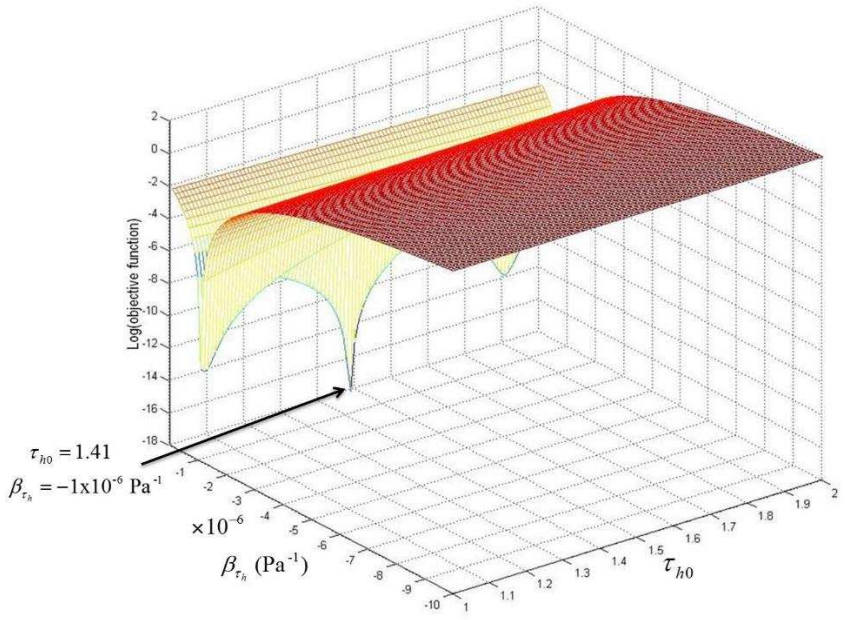

Figure 11. Results for the inversion with 2 parameters for: τ_{h0} and $\beta\tau_h$ with minimum corresponding to: τ_{h0}= 1.41 and $\beta\tau_h$= $-1.0\ \text{x}10^{-6}\text{Pa}^{-1}$. The z-axis shows the values of the objective function on a logarithmic scale.

Although not illustrated, we mention that the exact values $5.3\text{x}10^{-18}$ (m^2) and $-1.0\ \text{x}10^{-6}$(Pa^{-1}) were also obtained for $K_{\infty 0}$ and $\beta\tau_h$ in the case of noise free data, when inverting for these two parameters. However, when the inversion with 2 parameters is performed for $K_{\infty 0}$ and τ_{h0} even in the case of noise free data, a deviation from the exact solution is observed, namely: the values $K_{\infty 0}= 6.5\text{x}10^{-18}$ (m^2) and $\tau_{h0}= 1.15$ are obtained, with a relative error of 22.6% and 18.3%, respectively. This suggests that the two parameters $K_{\infty 0}$ and τ_{h0} are strongly correlated and hence difficult to obtain simultaneously. However, the product between the numerical values of $K_{\infty 0}$ and τ_{h0} is very close in value to the product between the exact values of $K_{\infty 0}$ and $\tau_{h0,}$ with a relative error of 0.15%, indicating that we can retrieve the product of $K_{\infty 0}$ and τ_{h0} by the inversion with two parameters, but not the exact individual values. In fact, from (2) and (3) one has

$$K_{\infty 0}\frac{\partial K}{\partial K_{\infty 0}} = K + \tau_{h0}\frac{\partial K}{\partial \tau_{h0}} \tag{53}$$

and since K is of $O(10^{-18})$ small, the normalised sensitivity coefficients for K_∞ and τ_h will appear indistinguishable. Another approach, proposed in Civan (2002, 2003, 2005), could be to modify the model to relate permeability to pore connectivity using a power-law flow unit equation, however this investigation is deferred to a future research work.

As for the inversion with 1 parameter, the inversion with 2 parameters was investigated for the case when noise is added to the direct problem solution, in the form given by Equation (51). **Table 3** shows the numerical results for $K_{\infty 0}$, τ_{h0} and $\beta\tau_h$ obtained when adding a noise of 0.1%.

Parameter combination	Parameter/unit	Exact	Numerical	Percentage error (%)
τ_{h0} and $\beta\tau_h$	τ_{h0}	1.41	1.51	6.7
	$\beta\tau_h$	$-1.0\text{x}10^{-6}$	$-1.0\text{x}10^{-6}$	0
$K_{\infty 0}$ and $\beta\tau_h$	$K_{\infty 0}$ (m^2)	$5.3\text{x}10^{-18}$	$7.3\text{x}10^{-18}$	37.7
	$\beta\tau_h$ (Pa^{-1})	$-1.0\text{x}10^{-6}$	$-9.0\text{x}10^{-7}$	10
$K_{\infty 0}$ and τ_{h0}	$K_{\infty 0}$ (m^2)	$5.3\text{x}10^{-18}$	$7.1\text{x}10^{-18}$	33.9
	τ_{h0}	1.41	1.12	20.4

Table 3. Results for inversion with noise for 2 parameters out of $K_{\infty 0}$, τ_{h0} and $\beta\tau_h$.

As expected, the relative error in this case is higher for both $K_{\infty 0}$ and τ_{h0}, namely it is 33.9% and 20.4%, respectively. However, when the product between the numerical values of $K_{\infty 0}$ and τ_{h0} is calculated, it can be observed that the relative error between this and the product between the exact value of $K_{\infty 0}$ and τ_{h0} is much smaller, namely it is 6.5%.

8.2.4. Inversion for 3 Parameters

For the inversion problem applied to 3 parameters, the previous arithmetic method of calculating the objective function (49) becomes prohibitive. In this case the minimisation of the nonlinear least-squares objective function (49) is performed numerically using the NAG routine E04FCF. This routine is a comprehensive algorithm for finding an unconstrained minimum of a sum of squares of a sum of squares of M nonlinear functions in N ($\leq M$) variables (see Gill and Murray, 1978). No derivatives are required. In our case N=3 and hence we require that $M \geq 3$.

The NAG routine E04FCF is applicable to problems of the form:

$$\text{minimise}\, F(\underline{X}) = \sum_{i=1}^{M}\left[f_i(\underline{X})\right]^2 \tag{54}$$

where $\underline{X} = (X_1, X_2, \ldots, X_N)$ and $M \geq N$.

The functions $f_i(\underline{X})$ are referred to as 'residuals' and are supplied as:

$$f_i(\underline{X}) = p(\underline{X}; 0, \bar{t}_i) - p(0, \bar{t}_i), \qquad i = 1, \ldots, M. \tag{55}$$

From an initial guess $\underline{X}^{(1)}$ supplied by the user, the routine generates a sequence of points $\underline{X}^{(k)}$, $k \geq 2$, given by

$$\underline{X}^{(k+1)} = \underline{X}^{(k)} + d^{(k)}\underline{p}^{(k)} \tag{56}$$

intended to converge to a local minimum of $F(\underline{X})$, where the vector $\underline{p}^{(k)}$ is a direction of search, and $d^{(k)}$ is chosen

such that $F\left(\underline{X}^{(k)} + d^{(k)}\underline{p}^{(k)}\right)$ is approximately a minimum with respect to $d^{(k)}$.

The numerical results for the inversion of the 3 parameters $K_{\infty 0}$, τ_{h0} and $\beta\tau_h$ are shown in **Table 4**, for a couple of initial guesses. The inversion for $K_{\infty 0}$ was done for 5.3 and the result was multiplied by 10^{-18}, for convenience in computing errors. The percentage errors are very small, showing some independence on the initial guess. However, for other initial guesses further away from the exact values, results may become trapped in a local minimum but this is typical with gradient search methods.

Parameter/unit	Exact	Numerical	Initial guess	Percentage error (%)
$K_{\infty 0}$ (m^2)	$5.3\text{x}10^{-18}$	$5.29\text{x}10^{-18}$	$7.0\text{x}10^{-18}$	0.236
		$5.44\ \text{x}10^{-18}$	$3.0\text{x}10^{-18}$	2.69
τ_{h0}	1.41	1.42	1.5	0.808
		1.38	1	2.06
$\beta\tau_h$ (Pa^{-1})	$-1.0\ \text{x}10^{-6}$	$-9.98\ \text{x}10^{-7}$	$-1.5\ \text{x}10^{-6}$	0.152
		$-9.98\ \text{x}10^{-7}$	$-0.5\ \text{x}\ 10^{-6}$	0.157

Table 4. Results for inversion of the 3 parameters $K_{\infty 0}$, τ_{h0} and $\beta\tau_h$ for exact data.

9. Laboratory Experimental Tests

The numerical approach was applied to experimental data obtained in the Wolfson multiphase flow laboratory at the University of Leeds for two samples: AB1 and AB2. The data for these two samples are presented in Appendix A. The gas used in our experiments is Helium, which does not absorb to shale. Consequently, the gas desorption data such as the Langmuir volume and pressure are set to zero. The intrinsic permeability of both these samples is expected to be very low. The modelled boundary conditions for both these examples are of the same type as the ones presented for Example 7.3, namely as given by (40)-(42). Laboratory results included measurements for the pressure at both the upstream and downstream boundaries. The direct problem was solved first for samples AB1 and AB2. Results were analysed for both the upstream and downstream boundary pressures for different values of the three unknown parameters, namely K_∞, τ_h and $\beta\tau_h$, for the initial 200 minutes of the experiment for AB1 and for the initial 60 minutes for AB2. To obtain a consistent value of the equilibrated pressure (pressure at which the upstream and downstream pressures become equal) with the value obtained by the laboratory experiments, the downstream volume was taken slightly smaller in the numerical calculations than in the laboratory experiments, namely it was taken to be $V_d=5.23\text{x}10^{-7}m^3$ for AB1 and $V_d=9.83\text{x}10^{-7}m^3$ for AB2. The compressibility coefficient for porosity β_ϕ and for intrinsic permeability $\beta_{K\infty}$ were determined for each sample, as described in Section 8.1.

Figure 12 illustrates the experimental results for the pressure at the upstream and downstream boundaries, in comparison with the numerical results obtained by solving the direct problem for $K_{\infty 0}= 5\text{x}10^{-22}m^2$ and $\beta\tau_h = -1.0\ \text{x}10^{-11}Pa^{-1}$ when using three different values for tortuosity τ_{h0}, namely: 2.5, 3 and 4. It is in evidence in this figure that the best estimates are obtained for $\tau_{h0} = 2.5$, when analysing the results for both the upstream and downstream boundary pressures. The fits of the pressure-pulse decay models to the experimental data are better near the initial and final times than in the middle portion of the time interval.

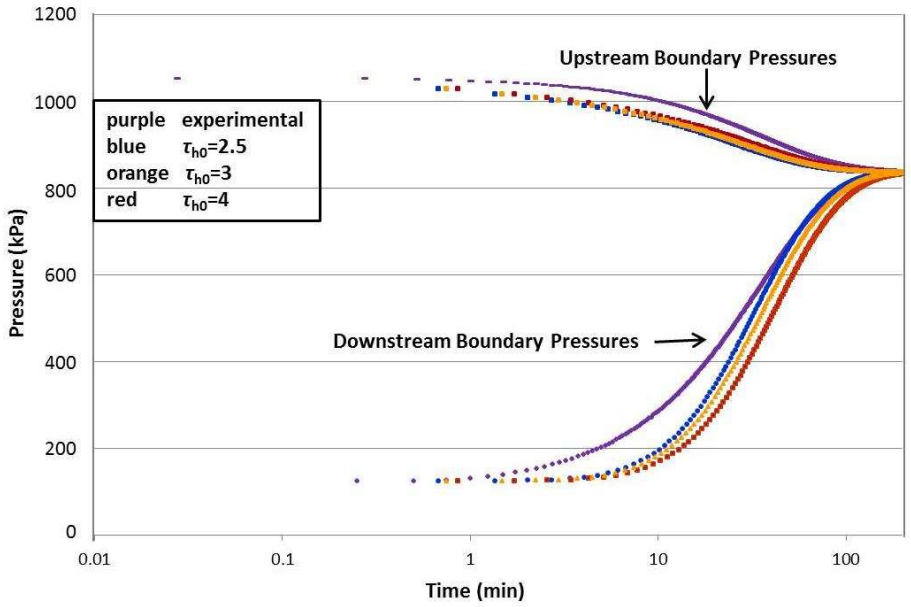

Figure 12. Upstream and downstream boundary pressures obtained experimentally and by solving the direct problem, when using K_{x0}= 5x10^{-22}m^2, $\beta\tau_{h0}$ = −1.0 x10^{-11}Pa^{-1} and $\tau_{h0} \in \{2.5, 3, 4\}$ for sample AB1, on a semi-log plot. (The upstream and downstream boundary pressures are shown in the same colour for each case, for consistency).

Figure 13 shows the experimental results for the pressure at the upstream and downstream boundaries for sample AB2, in comparison with the numerical results obtained by solving the direct problem for K_{x0}= 3x10^{-20}m^2 and $\beta\tau_h$= −1.0 x10^{-11}Pa^{-1} when using three different values for tortuosity τ_{h0}, namely: 3, 3.5 and 4.5. It is in evidence in this figure that the best estimates are obtained for τ_{h0} = 3.5, when analysing the results for both the upstream and downstream boundary pressures. As with sample AB1, the pressure pulse-decay model fits better the experimental data near the initial and final times than in the middle portion of the time interval.

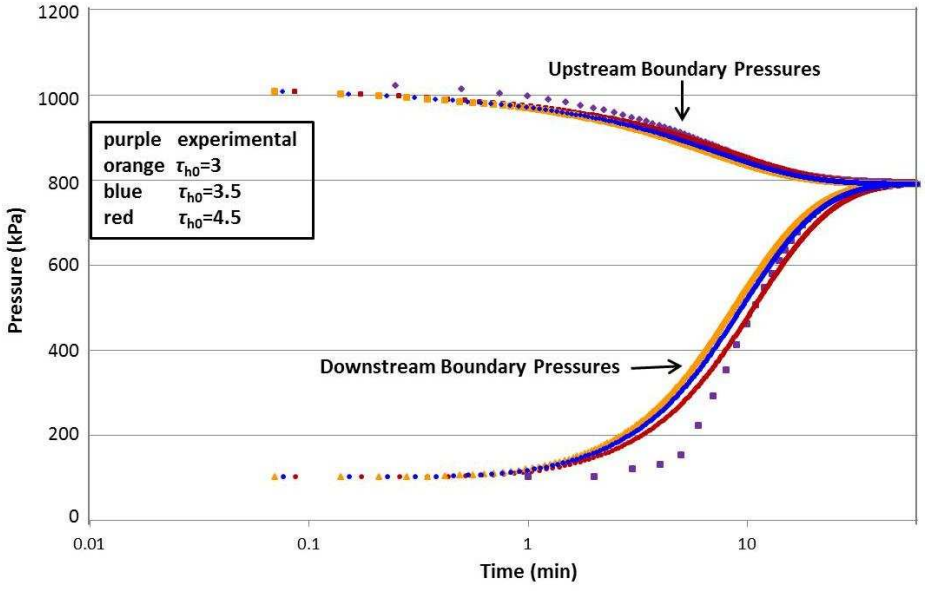

Figure 13. Upstream and downstream boundary pressures obtained experimentally and by solving the direct problem, when using K_{x0}= 3x10^{-20}m^2 and $\beta\tau_h$ = −1.0 x10^{-11}Pa^{-1} and $\tau_{h0} \in \{3, 3.5, 4.5\}$ for sample AB2, on a semi-log plot. (The upstream and downstream boundary pressures are shown in the same colour for each case, for consistency).

The inverse problem applied to three parameters has been investigated for samples AB1 and AB2, using the approach presented in Section 8.2.4. The initial guesses were taken close to the values of the three unknown parameters determined by the direct problem for the two examples. The inverse problem was first investigated when using one single set of experimental data per sample (i.e. data generated by running one laboratory test per

sample, using one single value for the initial upstream pressure and one for the initial downstream pressure). The inverse problem was also investigated when using two sets of experimental data per sample (i.e. data generated by running two different laboratory tests per sample, at different initial upstream and initial downstream pressures). In both cases however, the results obtained so far indicate that these three parameters are very difficult to retrieve together. This could be a result of combination of two key issues. Firstly, the nature of the relationship between $K_{\infty 0}$ and τ_{h0} (as mentioned earlier, they seem almost correlated and hence difficult to obtain simultaneously) needs to be further investigated, possibly changing the permeability model, as proposed in Civan (2002, 2003, 2005). This was somewhat expected, from the discussion presented for the inversion with noise for two parameters and the inversion with three parameters. Secondly, most shale samples that we have tested show evidence of a dual porosity system potentially a combination of fracture and matrix porosity. The one-dimensional formulation presented here does not account for such heterogeneity and therefore needs extending to two- or even three-dimensions.

10. Conclusions

A finite volume method has been developed to solve the nonlinear diffusion equation governing the pressure-pulse decay tests subject to appropriate initial and boundary conditions. The numerical approach was tested for different unsteady-state example problems for which analytical or numerical solutions are available and a very good agreement has been obtained. The method was then applied for solving the pressure-pulse decay tests given in Civan et al. (2011a, b) and a comparison with their results was made. An inverse problem was formulated to determine the values of the unknown parameters present in the governing equation. An inverse numerical solution has been presented for the inversion of up to three parameters. For the inversion of one and two parameters noise was also added to the direct problem pressure data and an error analysis was made. A very good retrieval of one of the unknowns was found for exact data. A reasonable retrieval of one of the unknowns was also obtained in the case of noisy data. When the inversion with two parameters is performed for $K_{\infty 0}$ and τ_{h0} even in the case of exact data, a deviation from the exact solution was observed, which indicated that these two parameters are almost correlated and hence difficult to obtain simultaneously. However, their product $K_{\infty 0}\,\tau_{h0}$ was correctly estimated.

Finally, our approach has been applied to practical laboratory pressure-pulse decay results obtained when using samples with very low permeability. Preliminary results, obtained by solving the direct problem and comparing the results with the experimental results for two samples, AB1 and AB2, indicate an intrinsic permeability of $O(10^{-22})$ and $O(10^{-20})$ for the samples, respectively. However, we were not able to invert for $K_{\infty 0}$, τ_{h0} and $\beta\tau_h$, simultaneously, from laboratory pressure-pulse decay tests using samples. The failure to invert for these three parameters potentially reflects the close correlation between $K_{\infty 0}$ and τ_{h0}. This is particular to the pressure-pulse decay test performed and, more importantly, that only the boundary pressure data have been used as additional measurement information in the inversion process. This obviously has the practical advantage that the inversion is non-intrusive; however, if better retrieval is desired then additional intrusive measurements of the pressure at internal ports mounted within the sample might be necessary (Lesnic et al., 1998). More general effects such as heterogeneity and anisotropy of the sample in the gas shale model will be investigated in a future work. Overall, the work presented in this paper may be used to test whether other gas flow models can be used to obtain the key unknowns of flow in shale from experimental data obtained in the laboratory.

Acknowledgements

The authors would like to acknowledge the financial support and samples supply received from Chevron, EBN and Nexen for this work, as part of the Shale Permeability Analysis (SHAPE) Project.

Nomenclature

A	empirical fitting constant (dimensionless)
A_i	coefficient used in the general boundary condition Equation (31) (dimensionless), i=0,1,2
b	slip coefficient (dimensionless)
B	empirical fitting constant (dimensionless)
B_0	coefficient used in the general boundary condition Equation (31) (dimensionless)
D	diameter of sample (m)
f(Kn)	flow condition function (dimensionless)

g	acceleration due to gravity (m^2/s)
$\mathbf{K}$	apparent permeability tensor of gas (m^2)
Kn	Knudsen number (dimensionless)
K_∞	intrinsic permeability (m^2)
L	length of sample (m)
M_g	molecular weight of gas (kg/kmol)
N_t	number of time steps (dimensionless)
N_x	number of control volumes (dimensionless)
$\mathbf{n}$	unit vector (dimensionless)
p	absolute gas pressure (Pa)
p_c	critical pressure (Pa)
p_d	downstream gas pressure (Pa)
p_L	Langmuir gas pressure (Pa)
p_s	scaling pressure (Pa)
p_u	upstream gas pressure (Pa)
$\bar{p}$	dimensionless gas pressure
$\bar{p}_{\text{noisy}}$	dimensionless gas pressure with added noise
$\bar{p}_{\text{numerical}}$	numerical dimensionless gas pressure
q	mass of gas adsorbed per solid volume (kg/m^3)
q_a	standard volume of gas adsorbed per solid mass (std m^3/kg)
q_L	Langmuir gas volume (std m^3/kg)
R_g	universal gas constant (8314 J/kmol K)
S_i	sensitivity coefficients
std	denotes standard conditions (273.15K and 101,325 Pa)
t	time (s)
$\bar{t}$	dimensionless time
T	absolute temperature (K)
T_c	critical temperature (K)
$\mathbf{u}$	volumetric flux vector ($m^3/m^2/s$)
V_b	bulk volume of core plug (m^3)
V_d	downstream reservoir volume (m^3)
V_p	effective pore volume (m^3)
V_{std}	molar volume of gas at standard temperature (273.15K) and pressure (101,325Pa) (std $m^3/kmol$)
V_u	upstream reservoir volume (m^3)
x	cartesian distance in the horizontal flow direction (m)
$\bar{x}$	dimensionless distance
Z	real gas deviation factor (dimensionless)

Greek

α	dimensionless rarefaction coefficient (dimensionless)

α_o asymptotic limit value of dimensionless rarefaction coefficient (dimensionless)

β ratio of compressive storage in the downstream reservoir to compressive storage in the upstream reservoir (dimensionless)

β_μ isothermal coefficient of compressibility for fluid viscosity (Pa^{-1})

β_ϕ isothermal coefficient of compressibility for porosity (Pa^{-1})

$\beta_{K\infty}$ isothermal coefficient of compressibility for intrinsic permeability (Pa^{-1})

β_ρ isothermal coefficient of compressibility for fuid density (Pa^{-1})

$\beta\tau_h$ isothermal coefficient of compressibility for tortuosity (Pa^{-1})

γ_u coefficient used in upstream boundary condition equations (dimensionless)

δt time step (dimensionless)

δx spatial step (dimensionless)

ε noise (dimensionless)

ε_n noise (percents)

$\mathbf{\Gamma}$ apparent diffusivity tensor (s)

Γ scalar apparent diffusivity (s)

$\bar{\Gamma}$ dimensionless scalar apparent diffusivity

ϕ porosity of porous media (fraction)

λ mean-free-path of molecules (m)

τ_h tortuosity of porous media (dimensionless)

ρ density (kg/m^3)

ϱ apparent flowing gas density (s^2/m^2)

$\bar{\varrho}$ dimensionless apparent flowing gas density

ρ_s material density of the porous sample (kg/m^3)

μ dynamic viscosity of gas (Pa s)

ν_d coefficient used in downstream boundary condition equations (dimensionless)

ν_u coefficient used in upstream boundary condition equations (dimensionless)

References

Al-Dhahir, A.A., Tan S.B. 1968. A Note on One-Dimensional Constant-Head Permeability Tests. Géotechnique, **18** (4), pp. 499–505.

Al-Anazi, B.D., Al-Quraishi, A.A. 2010. New Correlation for Z-Factor Using Genetic Programming Technique. Paper 128878-MS, Society of Petroleum Engineers. Paper presented at the SPE Oil and Gas India Conference & Exhibition, 20-22 January, Mumbai, India.

Banks, H. T., Dediu, S., Ernstberger, S. L. 2007. Sensitivity Functions and Their Uses in Inverse Problems. Journal of Inverse and Ill-Posed Problems, **15** (7), pp. 683–708.

Beskok, A., Karniadakis, G.E. 1999. A Model for Flows in Channels, Pipes, and Ducts at Micro and Nano Scales. Microscale. Thermophy. Eng. **3** (1), pp. 43–77.

Brace, W.F., Walsh, J.B., Frangos, W.T. 1968. Permeability of Granite under High Pressure. J. Geophys. Res. **73** (6), pp. 2225–2236.

Byrnes, A. P., Cluff, R.M., Web, J.C. 2009. Analysis of Critical Permeability, Capillary and Electrical Properties for Mesaverde Tight Gas Sandstones from Western U.S. Basins. DOE report DE-FC26-05NT42660

Chen T., Stagg, P.W. 1984. Semilog Analysis of the Pulse-Decay Technique of Permeability Measurement. Paper 11818-PA, Society of Petroleum Engineers. SPE Journal, **24** (6), pp. 639-642.

Civan, F. 2002. Relating Permeability to Pore Connectivity using a Power-Law Flow Unit Equation. Petrophysics **43**, No. 6,

pp. 457-476.

Civan, F. 2003. Leaky-Tube Permeability Model for Identification, Characterization, and Calibration of Reservoir Flow Units. Paper SPE-84603-MS, Society of Petroleum Engineers. SPE Annual Technical Conference and Exhibition, 5-8 October 2003, Denver, Colorado.

Civan, F. 2005. Improved Permeability Equation from the Bundle-of-Leaky-Capillary-Tubes Model. Paper SPE-94271-MS, Society of Petroleum Engineers. Paper presented at the SPE Production Operations Symposium, 16-19 April 2005, Oklahoma City, Oklahoma.

Civan, F. 2010. Effective Correlation of Apparent Gas Permeability in Tight Porous Media. Transport in Porous Media **82** (2), pp. 375–384.

Civan, F., Rai, C.S., Sondergeld, C.H. 2011a. Shale-Gas Permeability and Diffusivity Inferred by Improved Formulation of Relevant Retention and Transport Mechanisms. Transport in Porous Media **86** (3), pp. 925-944.

Civan, F., Rai, C.S., Sondergeld, C.H. 2011b. Shale Permeability Determined by Simultaneous Analysis of Multiple Pressure-Pulse Measurements Obtained under Different Conditions. Paper 144253-MS, Society of Petroleum Engineers. Paper presented at the North American Unconventional Gas Conference and Exhibition, 14-16 June 2011, The Woodlands, Texas, USA.

Civan, F., Rai, C. S., Sondergeld, C. H. 2012. "Determining Shale Permeability to Gas by Simultaneous Analysis of Various Pressure Tests," Paper 144253-PA, SPE Journal, Volume 17, Number 3, pp. 717-726.

Clennell, B. 1997. Tortuosity: A Guide Through the Maze. Geological Society, London, Special Publications **122**, pp. 299-344.

Cui, X., Bustin, A.M., Bustin, R. 2009. Measurements of Gas Permeability and Diffusivity of Tight Reservoir Rocks: Different Approaches and Their Applications. Geofluids **9**, pp. 208–223.

Dicker, A.I., Smits, R.M. 1988. A Practical Approach for Determining Permeability From Laboratory Pressure-Pulse Decay Measurements. Paper 17578-MS, Society of Petroleum Engineers. Paper presented at the International Meeting on Petroleum Engineering, 1-4 November 1988, Tianjin, China.

Esaki T., Zhang M., Takeshita A., Mitani Y. 1996. Rigorous Theoretical-Analysis of a Flow Pump Permeability Test. ASTM Geotechnical Testing Journal **19** (3), pp. 241 – 246.

Florence, F.A., Rushing, J.A., Newsham, K.E., Blasingame, T.A. 2007. Improved Permeability Prediction Relations for Low Permeability Sands. Paper 107954-MS, Society of Petroleum Engineers. Paper presented at the Rocky Mountain Oil and Gas Technology Symposium, 16-18 April 2007, Denver, Colorado, USA.

Freeman, C.M., Moridis, G.J., Blasingame, T.A. 2011. A Numerical Study of Microscale Flow Behavious in Tight Gas and Shale Gas Reservoir Systems. Transport in Porous Media **90**, pp. 253-268.

Gill, P.E., Murray, W. 1978. Algorithms for the Solution of the Nonlinear Least-Squares Problems. SIAM J. Numer. Anal. **15**, pp. 977–992.

Hsieh, P.A., Tracy, J.V., Neuzil, C.E., Bredehoeft, J.D., Silliman, S.E. 1981. A Transient Laboratory Method for Determining the Hydraulic Properties of 'Tight' Rocks–I. Theory. International Journal of Rock Mechanics and Mining Sciences and Geomechanics Abstracts **18** (3), pp. 245–252.

Jannot, Y., Lasseux, D., Laure Delottier, L., Hamon G. 2007. A Detailed Analysis Of Permeability and Klinkenberg Coefficient Estimation from Unsteady-State Pulse-Decay or Draw-Down Experiments. International Symposium of the Society of Core Analysts, Calgary, Canada, Paper SCA2008-09.

Jannot, Y., Lasseux, D., Laure Delottier, L., Hamon G. 2008. A Simultaneous Determination of Permeability and Klinkenberg Coefficient from an Unsteady-State Pulse-Decay Experiment. International Symposium of the Society of Core Analysts, Abu Dhabi, UAE, Paper SCA2008-09.

Javadpour, F. 2009. Nanopores and Apparent Permeability of Gas Flow in Mudrocks (shales and siltstone). J. Can. Pet. Technol. **48** (8), pp. 16–21.

Jones, S.C. 1972. A Rapid Accurate Unsteady-State Klinkenberg Permeameter. 3535-PA, SPE Journal, **12** (5), pp. 383-397.

Lesnic, D., Elliott, L., Ingham, D.B., Clennell, B., Knipe, R.J. 1997. A Mathematical Model and Numerical Investigation for Determining the Hydraulic Conductivity of Rocks. International Journal of Rock Mechanics and Mining Sciences **34** (5), pp. 741-759.

Lesnic, D., Elliott, L., Ingham, D.B., Knipe, R.J., Clennell, B. 1998. An Inverse Problem to Determine the Piecewise Homogeneous Hydraulic Conductivity within Rocks. Faulting. Fault Sealing and Fluid Flow in Hydrocarbon Reservoirs, (eds. G. Jones, Q. Fisher and R.J. Knipe), Geological Society London, Special Publications, Vol. **147**, pp. 261-268.

Lin, W. 1977. Compressible Fluid Flow Through Rocks of Variable Permeability. Rep. UCRL -52304, 15 Lawrence Livermore Lab., Livermore, California.

Loyalka, S.K., Hamoodi, S.A. 1990. Poiseuille Flow of a Rarefied Gas in a Cylindrical Tube: Solution of Linearized Boltzmann Equation. Phys. Fluids A **2** (11), pp. 2061–2065.

Luffel, D.L., Hopkins, C.W., Schettler Jr., P.D. 1993. Matrix Permeability Measurement of Gas Productive Shales. Paper 26633-MS, Society of Petroleum Engineers. Paper presented at the SPE Annual Technical Conference and Exhibition, 3-6 October, Houston, Texas.

Neuzil, C.E., Cooley, C., Silliman, S.E., Bredehoeft, J.D., Hsieh, P.A. 1981 A Transient Laboratory Method for Determining the Hydraulic Properties of 'Tight' Rocks–II. International Journal of Rock Mechanics and Mining Sciences and Geomechanics Abstracts. **18** (3), pp. 253–258.

Patankar, S.V. 1980. Numerical Heat Transfer and Fluid Flow. Series in Computational Methods in Mechanics and Thermal Sciences, Minkowycz and Sparrow Eds. (Mc Graw Hill).

Pong, K.C., Ho, C.M., Liu, J.Q., Tai, Y.C. 1994. Non-Linear Pressure Distribution in Uniform Micro Channels. Applications of microfabrication to fluid mechanics. In: ASMEFED **197**, pp. 51–56.

Ross, D.J.K., Bustin, R.M. 2007. Impact of Mass Balance Calculations on Adsorption Capacities in Microporous Shale Gas Reservoirs. Fuel **86** (17–18), pp. 2696–2706.

Roy, S., Raju, R., Chuang, H.F., Cruden, B.A., Meyyappan, M. 2003. Modeling Gas Flow Through Microchannels and Nanopores. J. Appl. Phys. **93** (8), pp. 4870–4879.

Sakhaee-Pour, A., Bryant, S.L. 2012. Gas Permeability of Shale. 146944-PA, SPE Reservoir Evaluation and Engineering **15** (4), pp. 401-409.

Shabro, V., Torres-Verdín, C., Javadpour, F. 2011a. Pore-Scale Quantification of Apparent Permeability and Electrical Resistivity of Hydrocarbon-Bearing Shale in the Presence of Gas Desorption. Society of Petrophysicists and Well Log Analysts (SPWLA) 52nd Ann. Logging Symposium, Colorado Springs, Colorado, May 14-18.

Shabro, V., Torres-Verdín, C., Javadpour, F. 2011b. Numerical Simulation of Shale-Gas Production: From Pore-Scale Modeling of Slip-Flow, Knudsen Diffusion, and Langmuir Desorption to Reservoir Modeling of Compressible Fluid. Paper 144355-MS. Paper presented at the North American Unconventional Gas Conference and Exhibition, 14-16 June, The Woodlands, Texas, USA.

Swami, V., Clarkson, C.R., Settari, A. 2012. Non-Darcy Flow in Shale Nanopores: Do We Have a Final Answer? Paper 162665-MS, Society of Petroleum Engineers. Paper presented at the SPE Canadian Unconventional Resources Conference, 30 October-1 November, Calgary, Canada.

Appendix A

Table A1. Data used for Pressure-Pulse Decay Tests.

Test	**Example 7. 5 (Test 2# Civan et al. 2011b)**	**Example 7. 6 (Test Civan et al. 2011a)**	**Experimental Test- Sample AB1**	**Experimental Test- Sample AB2**
Core Sample Properties				
Length L (m)	0.04057	0.05	0.0262	0.027077
Diameter D (m)	0.02528	0.05	0.0338	0.03657
Grain density ρ_s (kg/m^3)	2650	2500	2650	2650
Porosity ϕ (fraction)	0.0575	0.05	0.038	0.017
Gas Properties				
Gas type	Nitrogen	Methane	Helium	Helium
Viscosity μ (Pa s)	$1.8\text{x}10^{-5}$	$1.8\text{x}10^{-5}$	$1.984\text{x}10^{-5}$	$1.984\text{x}10^{-5}$
β_μ (Pa^{-1})	$8.388\text{x}10^{-9}$	$3.0\text{x}10^{-11}$	$1.68\ \text{x}10^{-9}$	$1.68\ \text{x}10^{-9}$

Molecular mass M_g (kg/kmol)	28.01	16	4	4
Critical temperature T_c (K)	126.2	190.6	5.2	5.2
Critical pressure P_c (Pa)	3,394,387.5	4,605,697.87	228,009.62	228,009.62
Molar volume of gas at standard temperature (273.15K) and pressure (101,325Pa) V_{std} (std m^3/kmol)	22.414	22.414	22.414	22.414
Pressure-Pulse Decay Tests Conditions				
Temperature T (K)	303.85	298.15	294.15	294.15
Initial gas pressure p_0 (Pa)	101,325	101,325	124,078.1	101,325
Upstream gas pressure p_{u0} (Pa)	3,546,375	500,000	1,051,753.8	1,020,879
Upstream reservoir volume V_u (m^3)	8.835 x10^{-6}	2.1 x10^{-5}	6.57x10^{-6}	6.57x10^{-6}
Downstream reservoir volume V_d (m^3)	1.1148 x10^{-5}	Not needed	1.83x10^{-6}	1.83x10^{-6}
Flow parameter values				
Intrinsic permeability $K_{\infty 0}$ (m^2)	1.97 x10^{-19}	5.3 x10^{-18}	Inverted	Inverted
Langmuir gas pressure p_L (Pa)	0	7.5 x10^6	0	0
Langmuir gas volume q_L (std m^3/kg)	0	0.01	0	0
Tortuosity τ_{h0} (dimensionless)	2.2	1.41	Inverted	Inverted
α_o constant (dimensionless)	1.358	1.358	1.358	1.358
A constant (dimensionless)	0.178	0.178	0.178	0.178
B constant (dimensionless)	0.4348	0.4348	0.4348	0.4348
Slip coefficient, b	−1	−1	−1	−1

β_ϕ (Pa^{-1})	9.8692 x10^{-12}	4.0 x10^{-6}	1.41 x10^{-9}	2.47 x10^{-9}
$\beta_{K\infty}$ (Pa^{-1})	3.947 x10^{-11}	1.0 x10^{-6}	7.61 x10^{-8}	1.19 x10^{-8}
$\beta\tau_h$ (Pa^{-1})	−1.9738 x10^{-11}	−1.0 x10^{-6}	Inverted	Inverted